# Fast scanning photothermal radiometry - towards in plane thermal characterization of micro structured devices

**Alejandro MATEOS-CANSECO**[1], **Andrzej KUSIAK**[1], **Jean-Luc BATTAGLIA**[1]

[1]I2M Laboratory, UMR CNRS 5295, University of Bordeaux
351 cours de la libération, 33400 Talence, France
*(Corresponding author: alejandro.mateos-canseco@u-bordeaux.fr)

**Abstract -** In this work, a fast photothermal radiometry with micrometric resolution is developed in order to enable the in-plane thermal characterization. The use of an optical arrangement allows the formation of the heating spot and measurement area at the same front sample surface. The heating spot of 6.6 $\mu$m in diameter is formed by focusing the laser; the measurement area of 12.5 $\mu$m in diameter is an image of the detector over the sample surface. The sample mounted over a translation stage permits its scanning with a micrometric precision. The use of modulated excitation allows exploring in a frequency range from 200 Hz up to 100 kHz. This technique is used to perform the thermal characterization of micro structured devices.

**Nomenclature**

| | | | |
|---|---|---|---|
| $A$ | signal amplitude, a.u | $\phi$ | phase lag, rad, degres |
| $M$ | emittance, $\mathrm{W/m^2}$ | $\rho C_p$ | volumetric heat capacity, $\mathrm{J/m^3K}$ |
| $P$ | power, W | $\varphi$ | flux,$\mathrm{W/m^2}$ |
| $R$ | measured signal | $\alpha$ | Hankel variable |
| $S$ | sensitivity function | $\epsilon$ | total hemispherical emissivity |
| $T$ | temperature, K | $\sigma$ | Stephan-Boltzmann constant |
| $W$ | width, m | $\omega$ | angular frequency, $rad$ |
| $k$ | thermal conductivity, $\mathrm{W/mK}$ | *Index and exponent* | |
| $r$ | radius, m | $m$ | measurement |
| $x, y, z$ | coordinate system axes | $det$ | infrared detector |
| *Greek symbols* | | $\infty$ | semi infinite media |
| $\theta$ | temperature frequency domain, $K$ | | |

## 1. Introduction

The continuous effort to improve the energy efficiency drives the development of new microstructured materials with enhanced thermal properties for a wide range of applications, from building thermal insulation [1, 2] to microelectronic application [3], where a key performance parameter is thermal conductivity. Moreover, assessment of heat transfer at microscale permits understanding behavior and design of different kinds of systems like microelectronic or micro-electro-mechanical devices with effective properties of composite materials. Thus, measurement of thermal properties of micro and nanostructured materials becomes an essential and challenging task.

One distinguish two main classes of methods for thermal characterization at micro-nanoscale: the contact and contactless methods. The main drawback of contact methods like SThM [4, 5], is the presence of the additional unknown parameters relating to the contact itself and the significant thermal inertia of the probes which limits its application to low frequency region. On

https://doi.org/10.25855/SFT2022-072

the other hand, the contactless methods are carried out without interaction probe-sample, allowing the study of faster dynamics. However, the contactless method are not suitable to achieve absolute temperature measurements.

One of these methods is the modulated photothermal radiometry (MPTR) which has been taken as the starting point for the development of a new scanning configuration setup. The photothermal radiometry [6] is a contactless and thus non-intrusive measurement technique designed for the thermal characterization of various types of materials and thin films. It is based on monitoring the emitted infrared radiation from the surface of the sample resulting from a photothermal periodic excitation provided by a laser. Along the years, the method has been improved in experimental and theoretical aspects [7, 8], and now a configuration of scanning photothermal radiometry at micrometric spatial resolution is presented in order to make it possible to study in-plane anisotropic thermal properties at frequencies above the limit of the infrared cameras which frame rate is limited to around 30 kHz for high speed cameras in sub-frame acquisition and several hundreds of Hz for most used cameras in full frame acquisition mode. Additionally, in the lock-in configuration a lower study frequencies have to be imposed to allow a good sampling [9–11].

## 2. Photothermal radiometry principle

Photothermal radiometry is based on monitoring the infrared radiation from the sample surface consequently to a photothermal excitation provided by a modulated laser. Considering a periodic heat flux $\varphi = \varphi_0 cos(\omega t)$ applied at the sample front face, the temperature increase of the sample is composed of a continuous and a transient part as: $\Delta T(t) = \Delta T_0 + \Delta T_\omega cos(\omega t + \phi)$. Assuming a weak enough disturbance, to produce a small temperature increase, the variation of the emitted radiation can be linearized as: $\Delta M \approx 4\epsilon\sigma\Delta T_0^3 \Delta T_\omega cos(\omega t + \phi)$. In this way it is possible to monitor the sample surface temperature $\Delta T$ by measuring the radiant emittance $\Delta M$, from the same excitation front face, with an infrared detector.

In a general manner, the signal recorded by the infrared detector, in frequency domain is: $R(j\omega) = A(\omega)e^{j\phi(\omega)}$. Where the amplitude, $A(\omega)$, is proportional to the emittance and thus, to the temperature variation $\Delta T_\omega$. Absolute temperature measurement requires a calibration process and knowing accurately the emissivity of the sample surface that comes to be a difficult task. Nevertheless, the phase-lag, $\phi(\omega)$, is sensitive to the sample thermal properties, this measurement is used as the explanatory variable within the parameter identification process.

## 3. Experimental Setup

### 3.1. Description of the setup

The experimental setup is presented in figure 1 with schematic representation on the right and the real implementation on the left. In this arrangement the three bands of the light spectrum are exploited: the visible spectrum (in green), the laser with wavelength, $\lambda = 1064$ nm (in yellow), and the emitted infrared radiation which maximum power is centered around $\lambda \approx 10$ $\mu$m (in red). The use of a reverse Cassegrain microscope objective with reflectance $> 96\%$ over 240 nm$-$20 $\mu$m wavelength operation region makes it possible to focus the laser beam over the sample surface and collect the emitted infrared radiation from the sample surface consequently to the periodic photothermal excitation. It makes it also possible to obtain the visible image of the sample surface.

Represented in yellow in figure 1, a continuous laser beam is sent through an acousto-optic

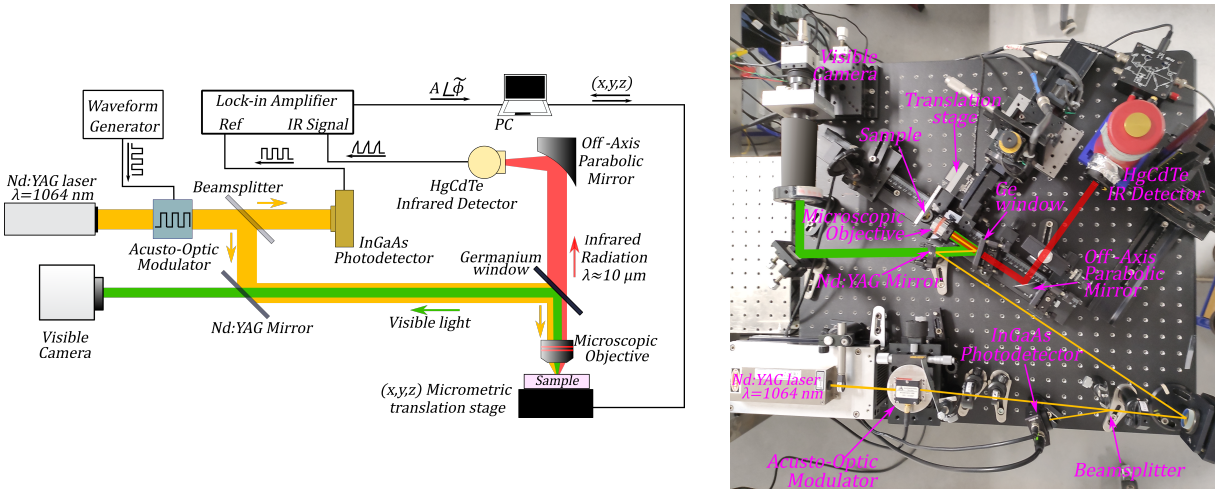


Figure 1 : *Schematic diagram of experimental setup (right). Real setup (left).*

(A-O) modulator to generate the periodic heat flux. A waveform generator drives the frequency, shape and amplitude of the A-O modulator. In order to avoid a possible phase lag due to the waveform generator and the acousto-optic modulator driver, a fast InGaAs photodetector is used as a reference for the measurements. After the A-O modulator a beamsplitter send a fraction of the laser to the photodetector and the rest is sent by a couple of windows/mirrors to the microscope objective which focuses the laser onto the sample surface. Illustrated in red, the emitted infrared radiation is collected by the microscope objective and sent through a germanium window, which filters the laser, to an off-axis parabolic mirror to focus it at the infrared detector. Finally in green, the visible light is collected by the microscope objective and reflected by the germanium window to go through Nd:YAG mirror, which is transparent for visible light, to reach the visible camera.

The measurement of the amplitude and phase lag between the disturbance (photodiode signal) and the IR radiation (detector) is performed using a lock-in amplifier. This device makes it possible to detect a signal drowned in a noise with high magnitude. In this way the phase lag measured by the lock-in amplifier, $\widetilde{\phi}(\omega)$, has only two contributions, the phase lag linked to the thermal response, $\phi(\omega)$, and the one generated by the infrared detector and associated amplifier, $\phi_{det}(\omega)$, whose function has to be calibrated (at $\lambda = 1064$ nm) to finally get the thermal phase lag as:

$$\phi(\omega) = \widetilde{\phi}(\omega) - \phi_{det}(\omega) \tag{1}$$

For the phase detector calibration, the HgCdTe sensor is placed in the path of the laser, between the beamsplitter and the Nd:YAG mirror, to be directly stimulated by the laser ( 1064 nm wavelength). With this configuration, using the InGaAs photodetector as reference, one can measure the phase lag, $\phi_{det}(\omega)$, introduced by the detection system.

A LabView based graphic user interface has been developed in order to manage the involved instrumentation and set the desired experimental conditions as well as collect and show the recorded information during the experiment.

### 3.2. The scanning system

The cartographic image formation from a pixel by pixel measurement made with the infrared sensor is achieved by scanning the sample surface. In the sweep process the sample

surface is displaced at constant velocity in the focal plane, perpendicular to the fixed laser beam propagation axis. For this, the sample is mounted over a 3-axis piezoelectric translation stage (P-611K101 from PI) with travel range to 100 $\mu$m $\times$ 100 $\mu$m $\times$ 100 $\mu$m. This precision displacement system is equipped with position sensors which allows to know the position of the plate while a feedback loop guarantees the exact and well repeatable positioning of the plate, thus avoiding a possible phenomenon of hysteresis.

### 3.3. Estimation of heating and measurement area

In order to know the spot diameter of the focused laser, the widely used knife edge method for beam characterization has been implemented. It allows quick, inexpensive and accurate determination of the beam parameters [12]. This technique consist in moving a knife edge perpendicular to the direction of propagation of the laser beam and record the total transmitted power as a function of the knife edge position. Assuming a laser beam with Gaussian distribution propagating along $z$ axis, the measured power and the knife-edge position are related by the error function as:

$$P(y) = \frac{1}{2}\left[1 - erf\left(\frac{\sqrt{2}(y - y_0)}{r_s}\right)\right] \tag{2}$$

Where $P$ is the power transmitted, $y$ is the knife-edge position, $y_0$ is the center position of the beam distribution and $r_s$ is the effective beam radius, at which the intensity drops at $1/e^2$ times the maximum value. The parameter $r_s$ can be found by fitting the equation 2 and the measured data. This measurement process was carried out for 25 points spaced at 1 $\mu$m along the propagation axis $z$, in the neighborhood of the focal plane of the microscope objective. The experimental configuration is represented in Figure 2. The $r_s$ obtained in function of the position $z$, follows a Gaussian beam propagation behaviour described as:

$$r_s(z) = r_0\sqrt{1 + \left(\frac{z - z_0}{b}\right)^2} \tag{3}$$

Where $r_0$ is the beam radius at the focal plane, also named beam waist, $z_0$ is the location of the focal plane and $b$ is the Rayleigh length, defined as the distance over which the beam radius spreads by a factor of $\sqrt{2}$. Figure 3 shows the measured beam propagation profile and the fitting curve with the equation 3 where the beam radius at the focal plane $r_0 = 3.3 \pm 0.034$ $\mu$m and Rayleigh length $b = 5.97 \pm 0.098$ $\mu$m were identified.

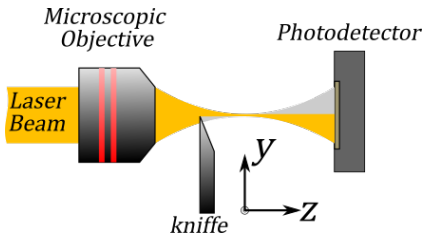


Figure 2 : *Schematic representation of Knife-edge method for Gaussian beam characterization.*

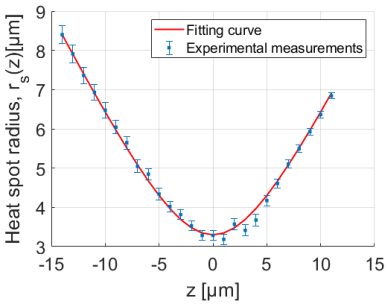


Figure 3 : *Beam radius measured and fitting curve at* $z_0 = 0$

About the measurement area, this is the one corresponding to the image of the sensor over the sample surface and to know it the magnification of the optical system was employed. The

sensing optical system is composed of two elements, the microscope objective with a focal length $f_o = 5$ mm and the off-axis parabolic mirror with a focal length $f_m = 200$ mm. Since the sample is placed at the focal length of the microscopic objective and the infrared detector is placed at the focal length of the off-axis parabolic mirror, the magnification of the optical system (from the sample to the sensor) is given by the ratio of the focal lengths, $m = f_m/f_o = 40$, that means the sensing area is 40 times smaller than the sensor size. As the HgCdTe sensor has a square active area with 500 $\mu$m width, one gets that the sensing area over the sample surface is a square with 12.5 $\mu$m width.

## 4. Validation on bulk sample

To test the experimental setup performance, a bulk stainless steel sample was used to run a thermal characterization study, with the thermal conductivity as a target property. The sample was placed at the focal plane, $z = 0$. To simplify the problem, the measurement area was considered as the circular area. Thereby, when a heat flux with Gaussian distribution of radius $r_0 = 3.3$ $\mu$m is applied at the sample surface, the average temperature over the aimed area of radius $r_m = 6.25$ $\mu$m is:

$$\bar{\theta}(j\omega) = \varphi_0 \frac{r_0^2}{2kr_m} \int_0^\infty \frac{e^{-\frac{\alpha^2 r_0^2}{8}} J_1(\alpha r_m)}{\sqrt{\alpha^2 + \frac{j\omega\rho C_p}{k}}} d\alpha \tag{4}$$

where $k$ and $\rho C_p$ are the sample thermal conductivity and volumetric heat capacity respectively and $J_1$ is the first kind Bessel function of order 1. With the phase-lag defined as: $\phi = arg(\bar{\theta})$, the thermal conductivity can be found by fitting the experimental data with the model.

The equation 4 allows to calculate the reduced sensitivity function of the phase, $S_P(a_i) = a_i \partial\phi/\partial a_i$, to the parameters $\boldsymbol{a} = [r_0, r_m, k]$. Figure 4 shows the sensitivity function of the phase for a frequency range from 200 Hz to 100 kHz, this is the frequency window at which the experiment can be completed. One can observe that the sensitivity to $r_0$ is almost constant and close to 0, that means higher tolerance to the spot radius perturbations in full frequency range. On the other hand, absolute value of the sensitivity to the measurement radius increase with the frequency and is always bigger than the sensitivity to the thermal conductivity, which makes the setup less tolerable to the out of focal measurements. In addition, figure 4 shows a correlation between $S_P(r_m)$ and $S_P(k)$, that means one can't estimate both parameters at same time, and the variations in measurement area will produce a different thermal conductivity value.

Figure 5 shows the experimental data and the fitting curve (using Levenberg-Marquardt algorithm). For the measurements frequency range a compromise had to be done between the frequency region for the best sensitivity and the region at which the signal was measured correctly, finally the 5 kHz - 50 kHz range was selected. In order to reduce the noise in the acquisition process, an statistical treatment was done by average several hundreds of measurements from the same point until reach the standard deviation lower to the 10 %, and each point is presented with its standard variation. However, it is clearly observed that residuals are not white, meaning the model is biased, that could be because the calibration has been made at the laser wavelength (1064 nm) that is not the working wavelength for the infrared detector (from 2 up to 12 µm). From the experiments a thermal conductivity $k = 14.17 \pm 1.12$ W/mK was found, which is consistent with the value measured by the Hot Disk method, $k = 14.45 \pm 0.98$ W/mK, for both methods $\rho C_p = 4 \times 10^6$ J/m$^3$K was used. In addition, in figure 5 is shown the phase lag, $\phi_{det}(\omega)$, introduced by the detector and the measurement chain.

In order to asses the tolerance with respect to out of focal measurements, the same experiment was carried out for $z = \pm 1, 2, 3, 4, 5\ \mu\mathrm{m}$. Figure 6 shows the estimated thermal conductivity versus the distance from the focal plane. One can observe that, in this configuration, for the region around 1 $\mu$m of the focal plane, the variation on the estimated thermal conductivity is lower than the standard deviation and represent only the $2\%$ of the central value.

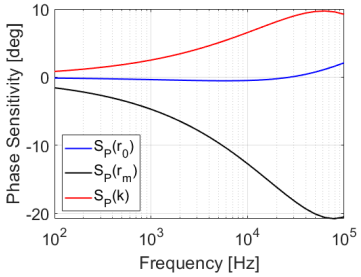


Figure 4 : *Phase Sensitivity function.*

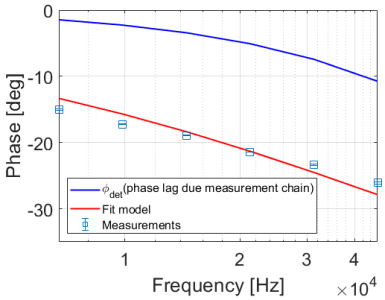


Figure 5 : *Thermal phase lag vs excitation frequency, from the stainless steel sample.*

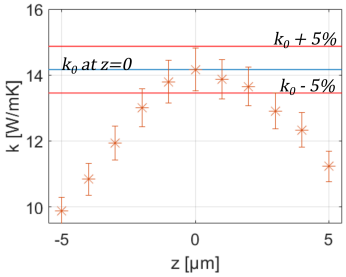


Figure 6 : *Thermal conductivity vs position in $z$.*

## 5. Scanning measurements

Once the experimental setup is validated on a bulk sample, image acquisitions have been performed in order to asses the possible resolution of the device. For this purpose, thin stripes from 3 omega method patterns were used. The strip is made of 400 nm Pt layer deposited over 400 nm $\mathrm{Ge} - \mathrm{Ge_2Sb_2Te_5}$ (GGST) layer, all over a Si substrate with 400 nm SiN layer. The schematic representation of the thin strip is presented in Figure 7.

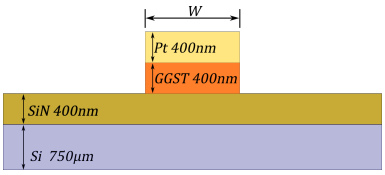


Figure 7 : *Cross section of 3 omega strip.*

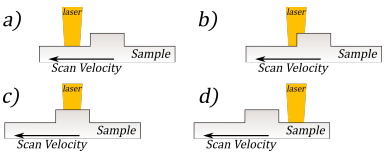


Figure 8 : *Line scanning process, from a) to d).*

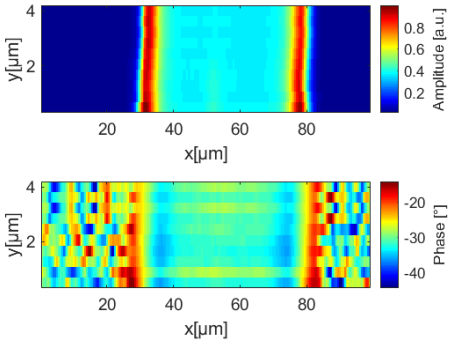


Figure 9 : *IR Image of 50 $\mu$m width strip over SiN-Si substrate.*

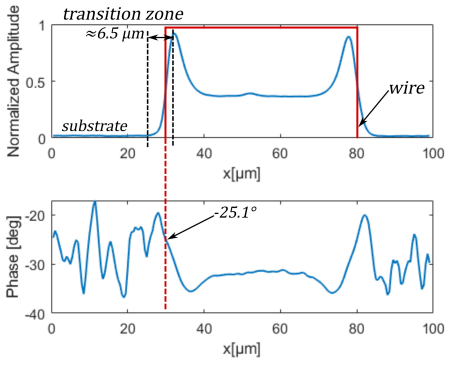


Figure 10 : *Normalized amplitude and phase lag at $y = 1$ $\mu$m.*

For the first scanning measurement, a strip with $W = 50$ $\mu$m width was used. The scanning area is 100 $\mu$m$\times$ 5 $\mu$m and one measurement (pixel) was taken each 0.5 $\mu$m while the sample

was traveling at 5 $\mu$m/s with a flux excitation at 99 kHz. Figure 8 shows the scanning process for one line. The lock-in acquisition time was set at 100 ms.

The scans of amplitude and phase measured are shown in Figure 9, where the 3 omega pattern is clearly visible in both amplitude and phase image. On the amplitude cross section shown in Figure 10, one can easily note the strip region raising over the substrate. Here, it is important to remember that this raising is not related to the height of the metallic region but to the change in the emittance and thermal properties. One can also identify a transition zone corresponding to the edge where the laser is over the substrate and the strip at same time, as shown in Figure 8-b), the width of this zone is estimated to be around 6.5 $\mu$m. Inside the strip zone, one can see that there is a variation between the central zone and the edge of the strip, that is probably due the heat confinement effect when the laser is close to the edge. On the phase cross section graphic (Figure 10) one can identify the same zones that in the amplitude plot, with the difference that the section corresponding to the substrate is mostly noisy. This is because the signal seems too low to be measured accurately, and contrary to the amplitude which values drop around zero, the phase is noisy.

To further challenge the resolution capabilities, one strip with 300 nm width was scanned. Figure 11 shows the obtained image. One more time, the contrast between the strip and the substrate is clearly visible, in both amplitude and phase. On the cross section, one can identify the region related to the strip, as a peak in the amplitude plot and a flat region in the phase plot, similar to those for the larger strip.

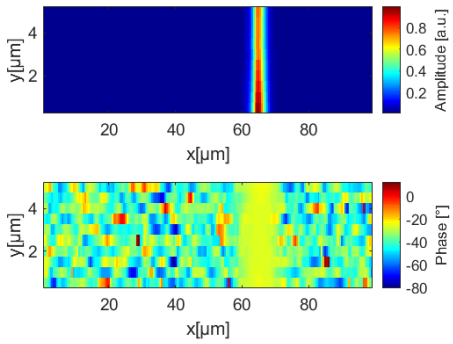


Figure 11 : *IR Image of 300 nm width strip over SiN-Si substrate.*

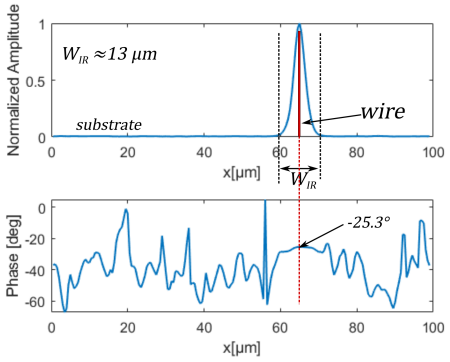


Figure 12 : *Normalized amplitude and phase lag at* $y = 1\ \mu$m .

One can observe also, that the width of the measured signal, $W_{IR}$ is much larger than the strip, the same widening phenomena occurs with the 50 $\mu$m strip (the transition zone at each side of the strip) but here it is more evident. It is important to remark that the phase measured on the narrow strip (-25.3° Figure 12) is the same as the phase measured at the edge of the 50 $\mu$m strip (-25.1° Figure 10), this suggests that the same two phenomena take place in the narrow strip, like in the edge region of the larger strip, modifying the measured signal with respect to the one measured in the center of the larger strip. On the 50 $\mu$m strip one can observe the change in the phase due to the heat confinement (before entering the transition zone) because it is large enough to allow the evolution when the laser approaches the edge, but in a smaller strip the heat is always confined like in the edge region of the larger strip. In the same way the narrow strip is always inside a transition zone that produces the widening effect, thus both phenomena lead to the obtained measurements although only one is evident for the narrow strip.

The widening effect of the transition zone, comes from the convolution phenomena between

the measurement area profile and the emittance sample profile. To explain this, one has to note that the temperature has a Gaussian distribution in the measured region. Therefore when scanning across the strip, there is a Gaussian profile displacing over a square profile and the measured signal is the pondered value. Thus, one obtains the convolution of the two signals. Figure 13 shows a simulated convolution between a Gaussian distribution with a radius of 6.25 $\mu$m as the temperature distribution and a square signal that represent the strip.

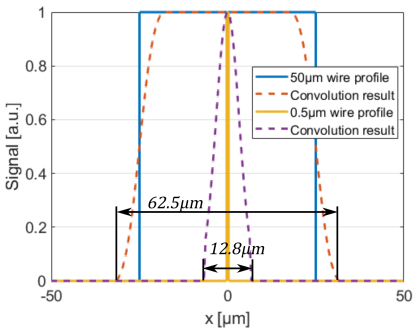


Figure 13 : *Convolution of a gaussian and step signals.*

The convolution effect shows the same widening behavior that is observed in figures 12 and 10 and the width of the convolution effect is consistent with the experimental results, giving a total width around 13 $\mu$m for the narrow strip and 63 $\mu$m for the larger strip. This permits to think that once knowing precisely the spatial function of the detector, the spatial deconvolution should allow to measure objects smaller than the measurement area with a good precision. In this way the ultimate resolution will be driven by the resolution of the translation stage of the scanning system.

## 6. Conclusion

A fast scanning photo-thermal radiometry setup for thermal analysis has been developed and validated on a bulk sample. It was shown that the device can perform accurate measurements located at its focal plane, with a tolerance of $\pm 1$ $\mu$m. From the scanning measurements, it is possible to extract information about the spatial pattern of the sample. Nevertheless, one has to be careful with the image interpretation and post processing because spatial convolution is not the only phenomena involved. As expected, the geometry plays an important role in the thermal response at this spatial scale.

The presented setup has shown the capability to detect sub-micrometric structured materials, if opaque, and perform fast measurements at high frequency. It has shown potential for the analysis of the edge effects on thermal distribution and for the study of constriction resistance and vertical contact resistance.

In future work, the integration of the experimental data with the finite element model will allow us to make a quantitative analysis and estimate the thermal properties of 3D structured samples.

### References

[1] Elodie Perros. *Caractérisation locale du transfert de chaleur aux interfaces solide-solide dans les milieux isolants*. PhD thesis, Université Paris sciences et lettres, 2017.

[2] Joris Doumouro. *Caractérisation de la laine de verre : étude des transferts de chaleur entre fibres de verre à l'échelle micrométrique*. Theses, Université Paris sciences et lettres, October 2020.

[3] Anna Lisa Serra. *Nouvelle génération de mémoire à changement de phase non volatile pour des applications à très basse consommation*. PhD thesis, Université Grenoble Alpes, 2021.

[4] A Majumdar, J P Carrejo, and J Lai. Thermal imaging using the atomic force microscope. *Applied Physics Letters*, 62(20):2501–2503, 1993.

[5] Séverine Gomès, Nathalie Trannoy, Françoise Depasse, and Philippe Grossel. A.C. scanning thermal microscopy: Tip–sample interaction and buried defects modellings. *International Journal of Thermal Sciences*, 39(4):526–531, 2000. ISSN 1290-0729. doi: https://doi.org/10.1016/S1290-0729(00)00232-5.

[6] Per-Erik Nordal and Svein Otto Kanstad. Photothermal radiometry. *Physica Scripta*, 20(5-6): 659–662, nov 1979. doi: 10.1088/0031-8949/20/5-6/020.

[7] Jean-Luc Battaglia, Andrzej Kusiak, and Kanka Ghosh. The use of photothermal techniques for thermal conductivity and thermal boundary resistance measurements of phase-change chalcogenides alloys. *Journal of Applied Physics*, 129(5):055106, 2021.

[8] B. Abad, D.-A. Borca-Tasciuc, and M.S. Martin-Gonzalez. Non-contact methods for thermal properties measurement. *Renewable and Sustainable Energy Reviews*, 76:1348–1370, 2017. ISSN 1364-0321. doi: https://doi.org/10.1016/j.rser.2017.03.027.

[9] Agustín Salazar, Arantza Mendioroz, and Alberto Oleaga. Flying spot thermography: Quantitative assessment of thermal diffusivity and crack width. *Journal of Applied Physics*, 127(13):131101, 2020. doi: 10.1063/1.5144972.

[10] Shrestha Ranjit, Kisoo Kang, and Wontae Kim. Investigation of lock-in infrared thermography for evaluation of subsurface defects size and depth. *International Journal of Precision Engineering and Manufacturing*, 16(11):2255–2264, 2015.

[11] Ranjit Shrestha and Wontae Kim. Evaluation of coating thickness by thermal wave imaging: A comparative study of pulsed and lock-in infrared thermography – part ii: Experimental investigation. *Infrared Physics & Technology*, 92:24–29, 2018. ISSN 1350-4495. doi: https://doi.org/10.1016/j.infrared.2018.05.001.

[12] Marcos A. de Araújo, Rubens Silva, Emerson de Lima, Daniel P. Pereira, and Paulo C. de Oliveira. Measurement of gaussian laser beam radius using the knife-edge technique: improvement on data analysis. *Appl. Opt.*, 48(2):393–396, Jan 2009. doi: 10.1364/AO.48.000393.